Measurements and Characterization of Turbulence in the Tip Region of an Axial Compressor Rotor

Yuanchao Li
Department of Mechanical Engineering,
Johns Hopkins University,
223 Latrobe Hall, 3400 N. Charles Street,
Baltimore, MD 21218
e-mail: yli131@jhu.edu

Huang Chen
Department of Mechanical Engineering,
Johns Hopkins University,
223 Latrobe Hall, 3400 N. Charles Street,
Baltimore, MD 21218
e-mail: hchen98@jhu.edu

Joseph Katz[1]
Department of Mechanical Engineering,
Johns Hopkins University,
122 Latrobe Hall, 3400 N. Charles Street,
Baltimore, MD 21218
e-mail: katz@jhu.edu

Modeling of turbulent flows in axial turbomachines is challenging due to the high spatial and temporal variability in the distribution of the strain rate components, especially in the tip region of rotor blades. High-resolution stereo-particle image velocimetry (SPIV) measurements performed in a refractive index-matched facility in a series of closely spaced planes provide a comprehensive database for determining all the terms in the Reynolds stress and strain rate tensors. Results are also used for calculating the turbulent kinetic energy (TKE) production rate and transport terms by mean flow and turbulence. They elucidate some but not all of the observed phenomena, such as the high anisotropy, high turbulence levels in the vicinity of the tip leakage vortex (TLV) center, and in the shear layer connecting it to the blade suction side (SS) tip corner. The applicability of popular Reynolds stress models based on eddy viscosity is also evaluated by calculating it from the ratio between stress and strain rate components. Results vary substantially, depending on which components are involved, ranging from very large positive to negative values. In some areas, e.g., in the tip gap and around the TLV, the local stresses and strain rates do not appear to be correlated at all. In terms of effect on the mean flow, for most of the tip region, the mean advection terms are much higher than the Reynolds stress spatial gradients, i.e., the flow dynamics is dominated by pressure-driven transport. However, they are of similar magnitude in the shear layer, where modeling would be particularly challenging. [DOI: 10.1115/1.4037773]

Introduction

Substantial effort, too large to summarize in a single paper, has already been made to characterize the structure of Reynolds stresses in turbomachines. Reviews covering different generations of modeling efforts are summarized, e.g., in Refs. [1–4]. While computational fluid dynamics (CFD), especially Reynolds-averaged Navier–Stokes (RANS) simulations, have become the primary tool for characterizing the flow in turbomachines, they raise questions about the applicability of the Reynolds stress models involved, and their impact on the flow dynamics [5]. The impact of different models has been assessed by comparing simulation results with experimental data at varying scales and levels of details, ranging from the blind CFD tests in the early 1990s [6] to recent comparison between particle image velocimetry (PIV) data and simulation results [7,8]. Several observations have been made, such as the required empirical tuning of constants [6], possible generation of negative normal stresses and associated realizability issues [9], the so-called stagnation point anomaly [10], model-dependent predictions [8,11], and turbulence anisotropy in contrast to k–ε models [8]. The latter could be resolved, e.g., by using full Reynolds stress transport models, or resort to large eddy simulations (LES). Application of fully resolved direct numerical simulation is not feasible at the present time, especially for industrial applications. Hence, as suggested in Refs. [5] and [12], RANS predictions need to be validated and calibrated based on experimental data.

Modeling of tip leakage flows is particularly challenging, where measured trends do not necessarily agree. For example, Lakshminarayana et al. [13] show that turbulence at the tip region is dominated by radial velocity fluctuations, presumably due to centrifugal effects, while experiments [14,15] and LES [16,17] in a linear cascade show higher wall-parallel velocity fluctuations. The cascade studies also show that shear is the dominant contributor to turbulence production around the tip leakage vortex (TLV). A recent comprehensive stereo-PIV (SPIV) data obtained in an axial waterjet pump by Wu et al. [18–20] show a very complex spatially nonuniform turbulence anisotropy, and both normal contraction/extension and shear contribute to turbulence production. These measurements have been performed in a refractive index-matched facility enabling unobstructed measurements of all the Reynolds stresses and terms affecting the turbulence production. The present paper extends this effort by examining the Reynolds stresses, parameters affecting them, and their relation to the strain rate tensor in the tip region of an axial compressor introduced in recent publications [21–29]. They provide detailed information about the formation, rollup, and breakup of the TLV, associated instabilities and mechanisms affecting the onset of stall [29], as well as the effects of flow rate and tip gap size on the tip region flow structure [28]. Here, the focus is the properties of turbulence in a selected midchord volume, where measurements performed in a series of closely spaced planes provide all components of the Reynolds stress and mean strain rate tensors. Specific reasons for the turbulence anisotropy are identified, followed by analysis of the stress–strain rate relations, and applicability of eddy viscosity-based models to the rapidly changing spatially varying strain rate field in the tip region. While the mean flow dynamics is dominated by the balance between acceleration and pressure gradients for most of the sample area, the spatial gradients in Reynolds stresses have comparable magnitudes in high shear regions, emphasizing their significance.

Experimental Setup

All the measurements have been performed in the JHU refractive index-matched facility discussed in detail in several recent

[1]Corresponding author.

Contributed by the International Gas Turbine Institute (IGTI) of ASME for publication in the Journal of Turbomachinery. Manuscript received August 3, 2017; final manuscript received August 18, 2017; published online September 26, 2017. Editor: Kenneth Hall.

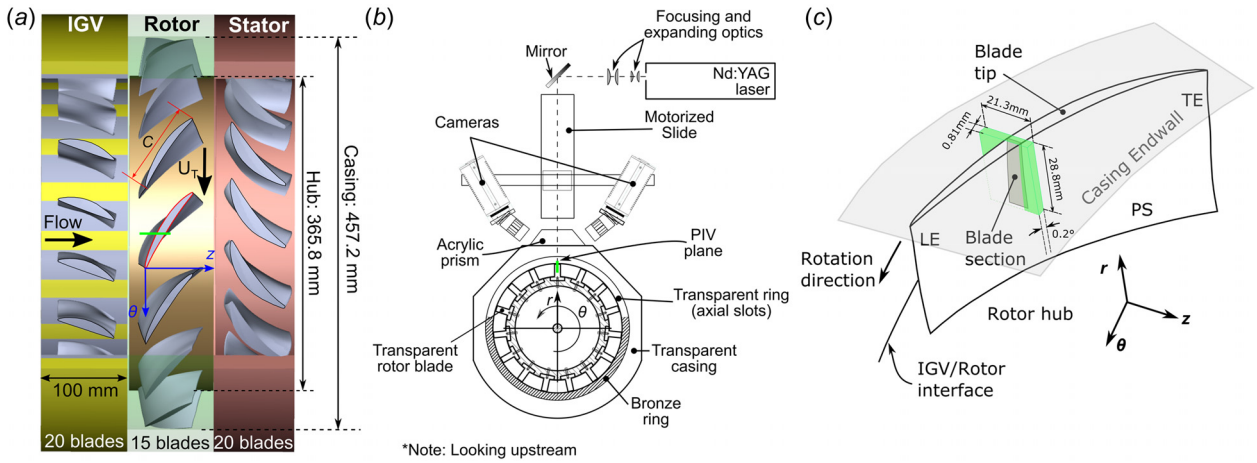

Fig. 1 (*a*) Three blade rows of the compressor, (*b*) experimental setup for SPIV measurements, and (*c*) the three-dimensional (3D) domain at $0.432 < s/c < 0.442$ containing 11 closely spaced meridional sample planes

publications, e.g., see Refs. [24] and [29]. Unobstructed optical access to the flow passages is achieved by using casing and blade rows made of transparent acrylic, and a fluid that has the same refractive index (1.49). This concentrated (62–63% by weight) aqueous solution of sodium iodide (NaI) has a specific gravity of 1.84 and a kinematic viscosity of 1.1×10^{-6} m^2/s in the relevant temperature range of 20–25 °C. The fluid properties, mean pressure, and pressure drop in the loop are monitored and controlled [24]. As illustrated in Fig. 1(*a*), the current compressor model consists of a row of inlet guide vanes (IGV) with 20 blades, a rotor with 15 blades and a stator with 20 blades. The blade shapes are derived from the first one and a half stages of the LSAC facility at NASA Glenn research center [22–24,30,31], but have a lower aspect ratio to facilitate measurements in the liquid. Relevant geometric parameters are provided in Table 1. The rotor blade investigated in the current study has a relatively large tip clearance of 2.4 mm, corresponding to 2.3% of blade chord length or 5.5% of the blade span. This tip clearance is determined directly by measuring the distance between the casing and blade tip from the PIV images, since a slight mismatch in refractive index leaves faint traces of the solid boundaries. The effects of tip clearance on the flow structure and distributions of turbulence intensity are discussed in previous papers [27,28]. The blade rows are housed in a thick transparent acrylic casing, with five flat surfaces allowing optical access from multiple views. All the tests discussed here have been performed at 480 RPM, resulting in the tip speed and Reynolds number specified in Table 1. A long channel upstream of the IGV is aimed at generating a nearly fully developed turbulent channel flow at the entrance to the test section. The measured velocity fluctuations, 12.7 mm upstream of the IGV and away from the wall, have a spatially averaged rms value of about 3.7% of the blade tip speed. This level is much lower than typical values measured in the blade tip region, as discussed in the Turbulence Intensity and Anisotropy section.

The machine performance is quantified using the static-to-static pressure rise coefficient, $\psi_{SS} = \Delta p/(0.5\rho U_T^2)$, and the flow rate coefficient, $\varphi = V_z/U_T$. Here, Δp is the pressure rise across the entire compressor measured using taps located upstream of the IGV and downstream of the stator. The flow rate is measured by translating a Pitot tube across the pipe in the return line and integrating the velocity profile. The uncertainties in pressure rise and flow rate measurements are about 1.2% and 1.7%, respectively [29]. The performance curve for current tip gap size is provided in Fig. 2, where the condition selected for the present study, $\varphi = 0.35$, is highlighted.

The data used in this paper are part of a large database obtained using SPIV for a smooth endwall casing. The experimental setup is shown in Fig. 1(*b*). The sample volume selected for the present analysis is illustrated in Fig. 1(*c*). It consists of a series of 11 closely spaced meridional planes centered around the chord fraction $s/c = 0.437$, and separated by $\Delta\theta = 3.6 \times 10^{-4}$ rad, corresponding to a circumferential distance between planes of 0.081 mm ($\Delta(s/c) = 9.2 \times 10^{-4}$) at the casing and 0.071 mm at the bottom of the field of view [29]. Here, s is a linear chordwise coordinate, with $s/c = 0$ located at the tip leading edge. The SPIV measurements are performed using a 1 mm thick, 200 mJ/pulse Nd:YAG laser sheet for illumination and a pair of PCO© 2000, 2048×2048 pixels, interline transfer cameras with 105 mm

Table 1 Geometric parameters of the test section

Casing inner diameter, D (mm)	457.2
Hub diameter, d (mm)	365.8
Rotor diameter, D_R (mm)	453.6
Rotor passage height, L (mm)	45.7
Rotor blade chord length, c (mm)	102.6
Rotor blade axial chord length, c_A (mm)	53.5
Rotor blade span, H (mm)	43.9
Rotor blade stagger angle, γ (deg)	58.6
Nominal tip clearance (mm)	1.8 (1.75%c)
Measured tip clearance, h (mm)	2.4 (2.3%c)
Shaft speed, Ω (rad/s) {RPM}	50.27{480}
Rotor tip speed, U_T (m/s)	11.47
Reynolds number, $U_T c/\nu$	1.07×10^6

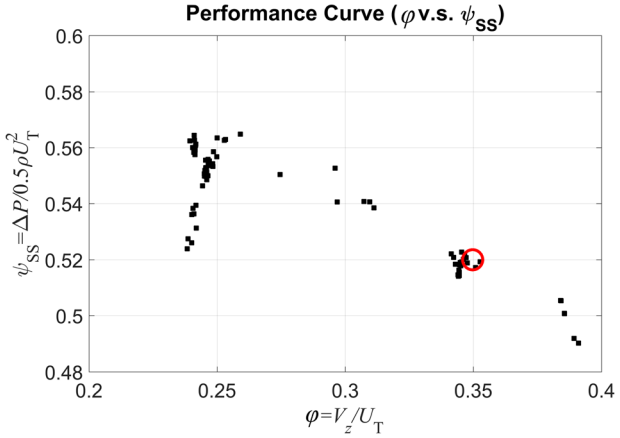

Fig. 2 Performance curve for the compressor with tip clearance of $h/c = 2.3\%$ and a smooth endwall. The operating condition for the present analysis is highlighted by a circle.

macrolenses for imaging. The lenses are inclined to the cameras by the Scheimpflug angle, and the sample areas are viewed through external prisms. The time delay between pulses is 20 μs. The flow is seeded with silver-coated, hollow, spherical glass particles, with an averaged diameter of 13 μm and a specific gravity of 1.6, slightly lower than that of the fluid. The image acquisition is synchronized with the rotor orientation using a shaft encoder.

Calibration of the SPIV images based on the two-step procedure of Wieneke [32] and image enhancement are discussed in Refs. [24] and [33]. The velocity is calculated using the commercial software LaVision© DaVis to conduct multipass cross-correlations with a final interrogation window of 32×32 pixels and 50% overlap. The field of view is 21.3×28.8 mm^2, and the vector spacing is 0.161 mm. Hence, the circumferential distance between planes is smaller than the in-plane vector spacing, facilitating 3D calculations of mean flow parameters [18,19,34]. One should note that the current vector resolution is not fine enough to resolve details of the boundary layers, but is capable of capturing the spatial variations of flow and turbulence parameters away from the walls. For each plane, the database consists of 2500 statistically independent instantaneous velocity distributions. The uncertainty in instantaneous velocity is about 2% [19,20,33,35]. Ensemble averaging reduces the uncertainty in mean velocity to about $1/\sqrt{2500}$ of the instantaneous values [28]. Ensemble-averaged velocity, vorticity, and Reynolds stress components are calculated for each plane using the 2500 realizations. A second-order central difference scheme is used for calculating the in-plane gradients of flow variables. A comparison of this approach to the results of a fourth-order central difference scheme shows agreement in the flow patterns, with less than 5% difference in magnitudes for most of the flow field, and 10–20% differences in regions of particularly high velocity gradients, e.g., the pressure side (PS) tip corner. The differences can be directly attributed to the limitations in spatial resolution in such areas. However, the circumferential derivatives ($\partial/\partial\theta$) are calculated using second-order polynomials fitted to the data points across multiple planes to alleviate the effects of jitter while matching the data obtained in different meridional planes.

Results and Discussion

The database obtained from ensemble averaging consists of spatial distributions of mean flow kinematic parameters and turbulence quantities. The former includes all components of velocity, vorticity, and strain rate tensor. The latter includes all the Reynolds stresses, and most (but not all) of the terms in the transport equation for turbulent kinetic energy (TKE) and Reynolds stresses. Some of these terms, e.g., the turbulence diffusion rate, involve third-order terms of the velocity fluctuations. They are presented in this section to elucidate trends in the TKE evolution, but a detailed investigation of their dynamics is beyond the scope of the present paper. A cylindrical coordinate system (r, θ, z) is used throughout this paper, with the origin located on the shaft centerline, and $z = 0$ and $\theta = 0$ coinciding with the blade tip leading edge. Results are presented using $r^* = (r - 0.5d)/L$ for the radial direction. Also, the analysis is performed in a rotating reference frame fixed to the blade, i.e., the blade rotation speed is already subtracted from the measured circumferential velocity.

Velocity and Vortical Structures in the Tip Region. The evolution of flow structures in the tip region of the present machine has been presented in multiple previous publications [24–29]. Hence, only features that are relevant to the analysis of turbulence properties are discussed briefly here. Figure 3(*a*) illustrates the 3D velocity distribution around the blade tip using a perspective view to highlight the variations in U_θ superimposed on the in-plane velocity vectors (U_z, U_r). The distributions of all three mean vorticity components, $\langle\omega_r\rangle$, $\langle\omega_\theta\rangle$, and $\langle\omega_z\rangle$, are provided in Figs. 3(*b*)–3(*d*), respectively. Characteristic relevant features can be summarized as follows: As the tip leakage flow passes through the tip clearance and rolls up into a TLV, it creates a complex 3D structure that involves all three vorticity components, but $\langle\omega_\theta\rangle$ is dominant (Figs. 3(*b*)–3(*d*)). Second, a shear layer with high $\langle\omega_\theta\rangle$, which is bounded by the backward leakage flow above and the forward main passage flow below, connects the TLV to the blade suction side (SS) tip corner (Fig. 3(*c*)). Near the SS tip corner, the axial and radial variations in U_θ result in an elevated $\langle\omega_r\rangle<0$, and the formation of two layers with opposite sign $\langle\omega_z\rangle$ (Fig. 3(*d*)), respectively. Third, elevated $\langle\omega_r\rangle$ with the expected signs can be observed in the boundary layers along the SS and PS of the blade (Fig. 3(*b*)). A boundary layer with $\langle\omega_\theta\rangle<0$ can also be seen along the casing endwall (Fig. 3(*c*)). Finally, as observed in a series of other axial turbomachines [19,20,36] as well as this compressor at different flow rates and tip gap sizes [26–29], a region with low circumferential velocity (protruding out in Fig. 3(*a*)) is located radially inward from the TLV center. The area of this region grows with s/c [26], and it represents a body of fluid swirling in the same direction of the blade, making it an integral part of the blade-induced blockage. The TLV center, as defined by the distributions of $\langle\omega_\theta\rangle$, is located in a region with sharp radial gradients in U_θ, resulting in $\langle\omega_z\rangle<0$. At low flow rates and in the aft part of the passage, the low U_θ area covers large portions of the tip region, and the associated velocity relative to the blade becomes very low. Propagation of associated instabilities also causes the onset of stall [29].

Turbulence Intensity and Anisotropy. The TKE distribution (Fig. 4(*a*)) is obtained by summing the three Reynolds normal stresses (Figs. 4(*b*)–4(*d*))

$$k = 0.5(\langle u_z'^2\rangle + \langle u_r'^2\rangle + \langle u_\theta'^2\rangle) \tag{1}$$

where the primes denote fluctuating quantities. Evidently, the turbulence is elevated in the vicinity of the TLV center and the shear layer connecting it to the blade SS corner. The TKE peak at the center corresponds to an average velocity fluctuation ($\sqrt{(1/3)\langle u_i' u_i'\rangle}$) of the order of $0.16U_T$, a significant fraction of which is associated with the interlacing large-scale vortical filaments [36]. Although their magnitudes and spatial distributions vary, these phenomena have appeared in all of the tip flow measurements that we have performed to date [25–29]. Hence, the present paper focuses on the dynamics involved and associated modeling issues. Common and distinct features in the distributions of TKE in the tip region for different tip gap sizes and operating conditions have already been discussed in previous papers [27,28]. However, for comparison purpose, two samples of TKE distributions, one for the narrow gap rotor ($h/c = 0.49\%$), but the same flow coefficient, and the other for the same tip gap, but at a lower flow rate ($\varphi = 0.25$), are provided in Figs. 5(*a*) and 5(*b*), respectively. In Fig. 5(*a*), the narrow gap results also show high turbulence in the TLV and in the shear layer, in agreement with the wide gap trends. They also indicate that the turbulence is elevated around the point of endwall boundary layer separation, in contrast to Fig. 4(*a*). For the narrow gap, the TLV entrains the negative $\langle\omega_\theta\rangle$ originating from the endwall boundary layer, and creates a negative vorticity layer that surrounds the TLV. Conversely, for the present wide gap, although the boundary layer separates from the endwall, it remains largely above the TLV, and generates a significantly lower turbulence level [28]. Also, the delayed rollup and breakup process of the TLV for this wide gap [28] confines the associated high TKE region to the vicinity of the TLV and the blade SS corner at the current s/c. In contrast, for the same geometry, but at a lower flow rate corresponding to the pre-stall condition ($\varphi = 0.25$ [29]), the turbulence level in Fig. 5(*b*) is substantially higher due to earlier TLV breakup, and the development of large-scale backflow vortical instabilities [28,29] that propagate from one blade to the next across the tip gap. These instabilities increase the TKE along the blade PS, in the tip

clearance, and even the SS of the next passage. Consequently, the turbulence level is much higher over the entire tip region under the prestall condition. The size and intensity of the vortical instabilities diminish, but do not vanish at $\varphi = 0.35$, resulting in a low TKE along the blade PS (Fig. 4(*a*)).

The spatial distributions of three Reynolds normal stresses (Figs. 4(*b*)–4(*d*)) show strong anisotropy, a common phenomenon for axial turbomachines, e.g., see Refs. [8], [18], and [19]. However, the dominant components are not necessarily the same [18]. Here, $\langle u'^2_z \rangle$ peaks in the shear layer, with a lower but elevated level in the TLV center, and $\langle u'^2_r \rangle$ dominates in the vicinity of the TLV center. The latter trend is consistent with Lakshminarayana et al. [13]. Elevated $\langle u'^2_\theta \rangle$ locates near the SS tip, and near the TLV center, but its magnitude is significantly lower than the other two components (note the difference in the scales). As in the

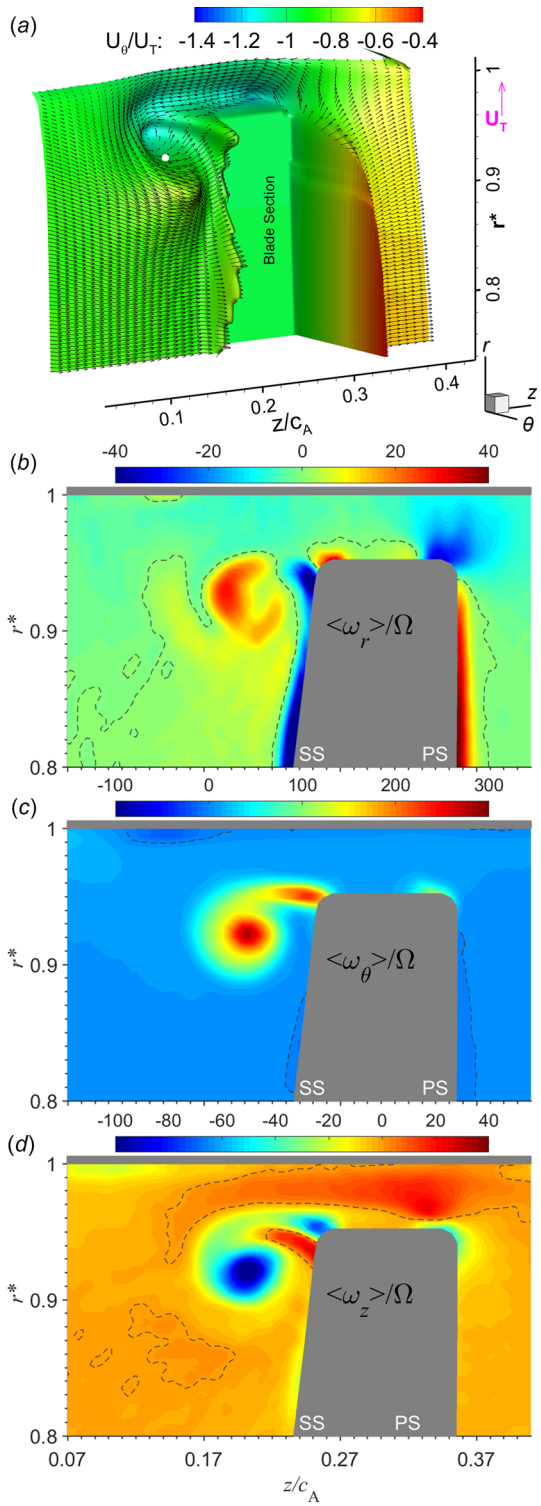

Fig. 3 (*a*) A perspective view illustrates the three-dimensional ensemble-averaged velocity distributions using vectors for the in-plane velocity (U_z, U_r), as well as elevation and contours for the out-of-plane velocity (U_θ) in a rotating reference frame. The vectors are diluted by 3:1 in the *z*-direction for clarity. A white dot marks the TLV center. (*b*)–(*d*) Distributions of the ensemble-averaged radial, circumferential and axial vorticity, respectively. The dashed lines follow the locations of zero values.

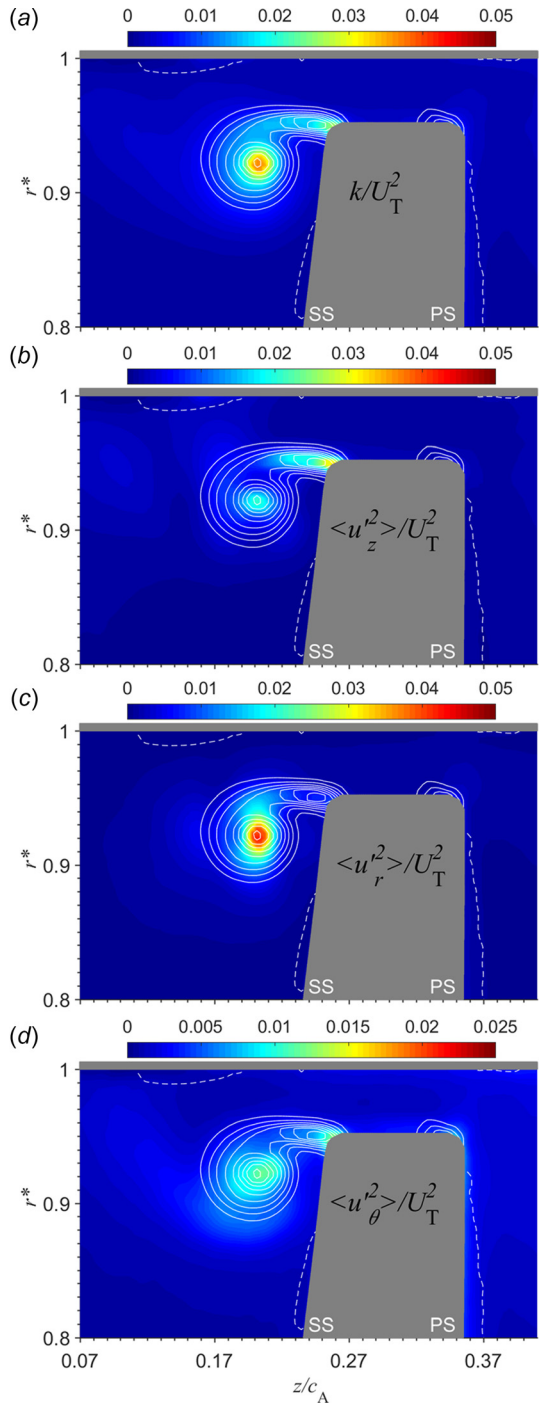

Fig. 4 Distributions of (*a*) TKE and three Reynolds normal stresses, (*b*) $\langle u'^2_z \rangle$, (*c*) $\langle u'^2_r \rangle$, and (*d*) $\langle u'^2_\theta \rangle$ for $\varphi = 0.35$ and *h*/*c* = 2.3%. The white contour lines show the distribution of $\langle \omega_\theta \rangle$.

assessment of RANS solvers by Liu et al. [8], full Reynolds stress transport models might be able to predict the existence of anisotropy around the TLV while most commonly used models assume isotropy, which is clearly incorrect for tip flows. The realizability of the Reynolds stress tensor has been assessed by calculating the eigenvalues and three invariants of the anisotropy tensor at every point, and by examining the spatial distribution of the anisotropy states based on how they fall in the "Lumley triangle" [37–39]. Results (not shown) demonstrate substantial spatial variability, but with some persistent trends. For example, turbulence dominated by one component occurs in the shear layer, nearly isotropic conditions appear in the main passage flow under the TLV, and two components with comparable magnitude appear in the high U_θ region. Addressing this topic in detail is deferred to future papers.

Turbulence Production and Transport. The anisotropy of normal stresses should be attributable to a significant extent to the differences in their production rates

$$P_{zz} = -2[\langle u_z'^2\rangle \partial_z U_z + \langle u_z' u_r'\rangle \partial_r U_z + r^{-1}\langle u_z' u_\theta'\rangle \partial_\theta U_z] \tag{2}$$

$$P_{rr} = -2[\langle u_r' u_z'\rangle \partial_z U_r + \langle u_r'^2\rangle \partial_r U_r + \langle u_r' u_\theta'\rangle (r^{-1}\partial_\theta U_r - r^{-1}U_\theta) - \langle u_r' u_\theta'\rangle r^{-1} U_\theta] + 4\Omega\langle u_r' u_\theta'\rangle \tag{3}$$

$$P_{\theta\theta} = -2[\langle u_z' u_\theta'\rangle \partial_z U_\theta + \langle u_r' u_\theta'\rangle \partial_r U_\theta + \langle u_\theta'^2\rangle (r^{-1}\partial_\theta U_\theta + r^{-1}U_r) + \langle u_r' u_\theta'\rangle r^{-1} U_\theta] - 4\Omega\langle u_r' u_\theta'\rangle \tag{4}$$

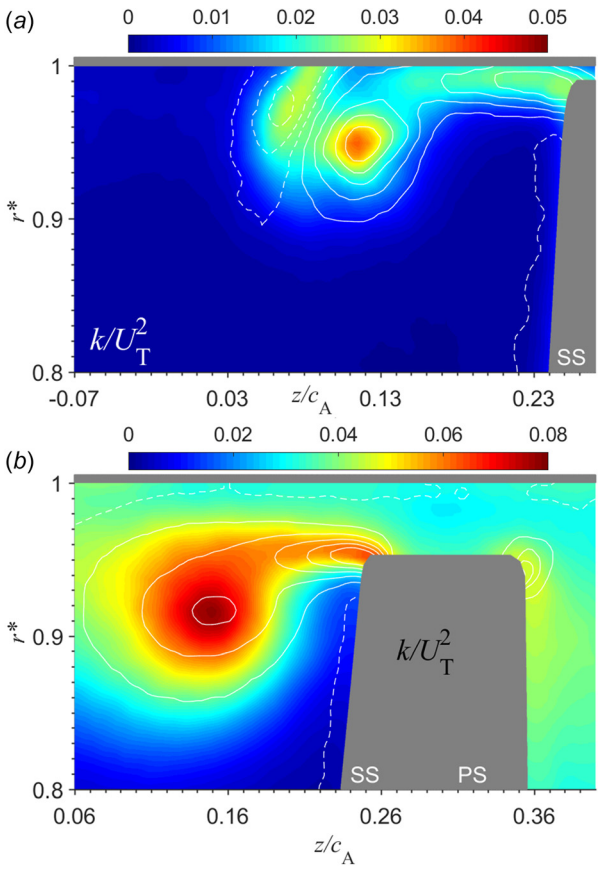

Fig. 5 Distributions of TKE for (*a*) $\varphi = 0.35$, $h/c = 0.49\%$ and (*b*) $\varphi = 0.25$, $h/c = 2.3\%$. The white contour lines show the distribution of $\langle\omega_\theta\rangle$.

These terms can be calculated completely by the present data. Use of a rotating reference frame adds additional terms to the production rates of $\langle u_r'^2\rangle$ and $\langle u_\theta'^2\rangle$, the magnitude of which depends on Ω. However, this Coriolis force effect is canceled for the production rate of TKE [18]

$$P = 0.5(P_{zz} + P_{rr} + P_{\theta\theta}) \tag{5}$$

Hence, the effect of rotation is to redistribute the turbulence energy among three normal stresses terms [1,40]. Instead of showing the total production terms, we opt to display the distributions of the most dominant contributors to each term and discuss the physical processes affecting them. The main contributors to the production of $\langle u_z'^2\rangle$, $\langle u_r'^2\rangle$, and $\langle u_\theta'^2\rangle$ are plotted in Figs. 6(*a*) and 6(*b*), 6(*c*) and 6(*d*), and 6(*e*) and 6(*f*), respectively. In measurements performed in a linear cascade [14,15], the dominant terms in TKE production are associated with the gradients of streamwise velocity. In the present compressor, the gradients of radial velocity are also major contributors to the production rate (Figs. 6(*c*) and 6(*d*)). Several phenomena are evident. First, consistent with the distribution of $\langle u_z'^2\rangle$, high shear production ($-2\langle u_z' u_r'\rangle \partial_r U_z$) occurs in the shear layer due to the large $\partial_r U_z$ there (Fig. 6(*b*)). Although the effect of this term is partially canceled by the negative region of $-2\langle u_z'^2\rangle \partial_z U_z$ shown in Fig. 6(*a*), corresponding to streamwise extension, the shear production still dominates. The peak of $\langle u_z'^2\rangle$ near the SS tip corner corresponds to combined effects of axial contraction ($-2\langle u_z'^2\rangle \partial_z U_z > 0$, Fig. 6(*a*)), the dominant term, and shear production ($-2\langle u_z' u_r'\rangle \partial_r U_z$).

Second, interestingly, Figs. 6(*b*) and 6(*c*) indicate that the TLV center is affected by two shear production terms of similar shapes and magnitudes, but with opposite signs. The first, $-2\langle u_z' u_r'\rangle \partial_r U_z$ is positive and affects P_{zz}, and the second, $-2\langle u_r' u_z'\rangle \partial_z U_r$ is negative and affects P_{rr}. Since they share the same Reynolds shear stress term, their net effect is a transfer of energy from $\langle u_r'^2\rangle$ to $\langle u_z'^2\rangle$ in a flow domain where the circumferential vorticity $\langle\omega_\theta\rangle = \partial_z U_r - \partial_r U_z$ is high and the corresponding shear strain rate is low, consistent with being located near the vortex center. Hence, this energy transfer is inherent to being located in a high vorticity region where the Reynolds stress is high. Similar trend has been found in other turbomachines [18]. Such an energy transfer might be able to explain the weak but distinct peak of $\langle u_z'^2\rangle$ near the TLV center, in contrast to the high $\langle u_r'^2\rangle$ there. Furthermore, the sink for $\langle u_r'^2\rangle$ ($-2\langle u_r' u_z'\rangle \partial_z U_r < 0$) is largely balanced by a bigger radial contraction source term $-2\langle u_r'^2\rangle \partial_r U_r$ near the vortex center (Fig. 6(*d*)). The radial contraction is also high in the shear layer, where it is not opposed by other terms. Yet, $\langle u_r'^2\rangle$ is low there indicating that other transport terms are involved. Interestingly, near the TLV center, $-2\langle u_z'^2\rangle \partial_z U_z$ (Fig. 6(*a*)) and $-2\langle u_r'^2\rangle \partial_r U_r$ (Fig. 6(*d*)) are divided into four quadrants and have opposite signs since stretching of one velocity components co-occurs with contraction of the other. Hence, they partially cancel each other in the TKE production (but not components). Similar patterns have been observed in the LES of linear cascades [16].

Third, consistent with the much weaker $\langle u_\theta'^2\rangle$, its production terms (Figs. 6(*e*) and 6(*f*)) are significantly smaller than those of the other components. The main contributor is the circumferential shear production, $-2\langle u_r' u_\theta'\rangle \partial_r U_\theta$, shown in Fig. 6(*e*). However, there are also obvious places where trends of the stress and the production are quite different. For example, both main contributors cannot explain the high $\langle u_\theta'^2\rangle$ around the SS tip corner, indicating that either transport terms or pressure-driven intercomponent transfer from the other terms are important. Also, the present circumferential contraction term (Fig. 6(*f*)) is very small. However, as shown for another axial pump [18], this term is significant during TLV breakup, which, for the present machine, occurs at higher s/c [28]. In summary, several trends in the spatial nonuniformity

and anisotropy of Reynolds normal stresses can be explained by examining the corresponding local production rate terms. However, some of the trends are inconsistent, requiring a more comprehensive examination of the entire transport equations, accounting for the effects of advection by mean flow, turbulent diffusion, pressure–strain correlation, and dissipation.

The evolution equation for TKE can be written as

$$\partial_t k = \Pi + P + A + T + M - \varepsilon \tag{6}$$

where Π is the pressure diffusion, A is the mean-flow advection rate, T is the turbulent diffusion rate, M is the viscous diffusion rate, and ε is the dissipation rate. They are defined as follows:

$$\Pi = -\rho^{-1}(\partial_z\langle p'u'_z\rangle + \partial_r\langle p'u'_r\rangle + r^{-1}\langle p'u'_r\rangle + r^{-1}\partial_\theta\langle p'u'_\theta\rangle) \tag{7}$$

$$A = -(U_z\partial_z k + U_r\partial_r k + r^{-1}U_\theta\partial_\theta k) \tag{8}$$

$$T = -0.5(\partial_z\langle qu'_z\rangle + \partial_r\langle qu'_r\rangle + r^{-1}\langle qu'_r\rangle + r^{-1}\partial_\theta\langle qu'_\theta\rangle), \quad (q = u'^2_z + u'^2_r + u'^2_\theta) \tag{9}$$

$$M = \nu\nabla^2 k + \nu\frac{\partial^2\langle u'_i u'_j\rangle}{\partial x_i \partial x_j} \tag{10}$$

$$\varepsilon = 2\nu\langle S'_{ij}S'_{ij}\rangle \tag{11}$$

Of these terms, the present data cannot be used for calculating Π. However, recently introduced techniques, which involve time-resolved 3D velocity measurements, are already being used for calculating the instantaneous pressure distributions in simpler turbulent flows [41–45]. Also, the spatial resolution of the present data is not sufficient for calculating ε without significant attenuation. Hence, in the following analysis, it is denoted as ε^*. Distributions of P, A, T, ε^*, and M are provided in Figs. 7(*a*)–7(*e*), respectively. Figure 7(*a*) demonstrates that the production rate is positive and high in the shear layer, and in parts of the TLV center. These trends are consistent with the distribution of TKE in the shear layer, but only in part for the TLV center. In some areas, P is negative, e.g., below the shear layer. Such a phenomenon might occur under nonequilibrium conditions, e.g., when the direction of mean strain rate changes rapidly, and the turbulence does not respond fast enough. As an example, we have shown that it occurs around the leading edge of a rotor intersecting an IGV wake [46]. For the present machine, the region containing the TLV and the shear layer involves rapid spatial variations in flow directions (see Fig. 3(*a*)). Hence, the associated strain rates vary significantly along the path of vortical filaments entrained into the TLV. It begins with axial extension ($S_{zz} > 0$) and radial compression ($S_{rr} < 0$) along the shear layer, but switches to radial extension ($S_{rr} > 0$) and axial compression ($S_{zz} < 0$) when the leakage flow meets the passage flow and separates. Then, the filaments travel through a region with radial compression and axial stretching while following the passage flow, followed by another change in normal strain rate direction to radial stretching and axial compression when the blade SS is approached. Since these changes occur over a short distance, it is unlikely that equilibrium conditions could be reached. As shown later, the shear strain rates also vary significantly in space and as a result, their magnitudes and signs are not always consistent with those of the shear stresses, also contributing to the nonequilibrium condition and generation of negative production rates in certain areas.

The advection by mean flow term shown in Fig. 7(*b*) has comparable order of magnitude as P. The high advection rate is mostly associated with axial ($-U_z\partial_z k$) and circumferential ($-r^{-1}U_\theta\partial_\theta k$) transport. The latter is affected by performing the analysis in a rotating reference frame, and its values are not necessarily high in a stationary frame. The turbulent transport term (Fig. 7(*c*)) is elevated in the TLV and the shear layer, but is for the most part smaller than P or A. Around the TLV center, this diffusion term is divided into four quadrants. Further decomposition (not shown) shows comparable contributions from all the four terms involved in Eq. (9), but with differences in spatial distributions and signs. As one might expect, in regions of high TKE production, e.g., near the TLV center and the SS corner, the mean advection and turbulent transport terms are negative, implying that the turbulence is transported to other areas. The viscous diffusion term M (Fig. 7(*e*), note the difference in scales) is significantly smaller than the aforementioned ones.

Accurate estimation of the dissipation rate from experimental data is challenging, especially in the inherently inhomogeneous

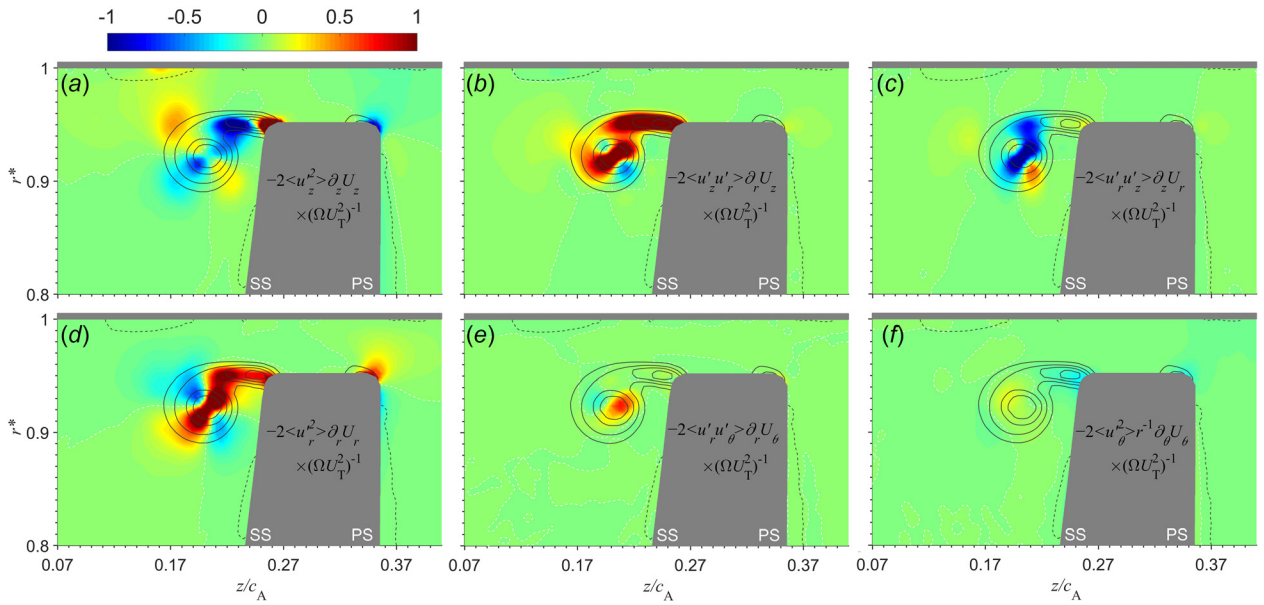

Fig. 6 Dominant terms in the production rate of Reynolds normal stresses: (*a*) $-2\langle u'^2_z\rangle\partial_z U_z\,(\Omega U_T^2)^{-1}$, (*b*) $-2\langle u'_z u'_r\rangle\partial_r U_z\,(\Omega U_T^2)^{-1}$, (*c*) $-2\langle u'_r u'_z\rangle\partial_z U_r\,(\Omega U_T^2)^{-1}$, (*d*) $-2\langle u'^2_r\rangle\partial_r U_r\,(\Omega U_T^2)^{-1}$, (*e*) $-2\langle u'_r u'_\theta\rangle\partial_r U_\theta\,(\Omega U_T^2)^{-1}$, and (*f*) $-2r^{-1}\langle u'^2_\theta\rangle\partial_\theta U_\theta\,(\Omega U_T^2)^{-1}$

turbomachinery flows. Several factors affect the accuracy of typical methods, most importantly a spatial resolution of about two Kolmogorov length scales are required for fully resolving the small-scale velocity gradients [47,48]. A coarser resolution rapidly attenuates the dissipation rate. For the current study, the spatial resolution of the measurements is much larger than the Kolmogorov length scale. Also, some of the instantaneous out of plane derivatives are missing, requiring an assumption of small-scale isotropy [49]. Therefore, ε^* based on Eq. (11) is highly underestimated, resulting in a production rate that is 50–100 times higher over a broad area. In well resolved systems, they should have similar magnitudes.

As mentioned earlier, the pressure diffusion term is not available for the present database (future studies will). However, some of the trends of the pressure diffusion term could be roughly estimated from a balance involving the other terms. Neglecting the unsteadiness caused by the IGV wakes (which is questionable), the TKE is time-independent in the rotor reference frame ($\partial_t k = 0$). Hence, Π can be estimated from

$$-\Pi^* = P + A + T + M - \varepsilon^* \tag{12}$$

where the Π^* is added to denote the effect of the underestimated ε^*. The result is plotted in Fig. 7(*f*). In the shear layer, $-\Pi*$ changes sign from high positive values in the upper part, which originates from the production rate, to high negative values in the bottom half, which originates from the mean advection. One should also notice that if the same analysis would be performed using a much higher and more realistic dissipation rate (which is always positive), the negative region in Fig. 7(*f*) would expand, and could not be balanced by any other term except for pressure diffusion. High levels of pressure–velocity correlations, hence pressure diffusion, should be expected for a flow impinging on a solid wall [42].

A Discussion on the Eddy Viscosity Models. The availability of the complete Reynolds stress and mean strain rate tensor enables direct validations of the eddy viscosity concept and associated models. The first possible approach for evaluating the eddy viscosity (ν_T) is based on the turbulence production term [50], namely,

$$P = -\langle u_i' u_j' \rangle \boldsymbol{S}_{ij} = 2\nu_{T,P} \boldsymbol{S}_{ij} \boldsymbol{S}_{ij} \tag{13}$$

The distribution of $\nu_{T,P}$, provided in Fig. 8, displays substantial spatial variation both in sign and magnitude. Particularly, high positive values are measured around the TLV center due to the high production rate and unmatched levels of strain rate there. Conversely, in the shear layer, the strain rate is substantially higher, resulting in a much lower $\nu_{T,P}$. In the tip gap, the eddy viscosity is largely negative, with particularly high values above the blade tip and along the endwall, both due to low strain rates there. The eddy viscosity is also negative along the PS and SS of the blade. Existence of a negative eddy viscosity, an obvious indicator of nonequilibrium conditions, is not considered in the turbulence models applied in common CFD practices.

The eddy viscosity can also be obtained from the stress–strain rate relation directly

$$\boldsymbol{R}^D_{\alpha\beta} = -\langle u_\alpha' u_\beta' \rangle + \frac{2}{3} k \delta_{\alpha\beta} = 2\nu_{T,\alpha\beta} \boldsymbol{S}_{\alpha\beta} \tag{14}$$

(Greek letters indicate no summation.) As a demonstration of its extreme variability and inconsistency, Fig. 9 shows the distributions of three shear strain rates, the corresponding Reynolds shear stresses, and the resulting eddy viscosity values obtained for each component. Numerous observations can be made from these plots. For instance, the high negative $\boldsymbol{S}_{rz}$ and $-\langle u'_z u'_r \rangle$ in the shear layer result in a high shear production rate (Fig. 6(*b*)) and a positive $\nu_{T,rz}$. However, in other areas, the values of eddy viscosity change sign and fluctuate over many orders of magnitude. In particular, around the TLV center, the shear strain rates are distributed in a spatial pattern of four quadrants with opposite signs, but the Reynolds shear stresses do not have a similar pattern, indicating lack of functional correlation, which results in sharp variations in sign and magnitude. One obvious example is the positive $\boldsymbol{S}_{z\theta}$ and negative $-\langle u'_z u'_\theta \rangle$ in the TLV center, resulting in high negative eddy viscosity in this area.

Following Schmitt [51], one can use the ratio indicator ρ_{RS}, defined as

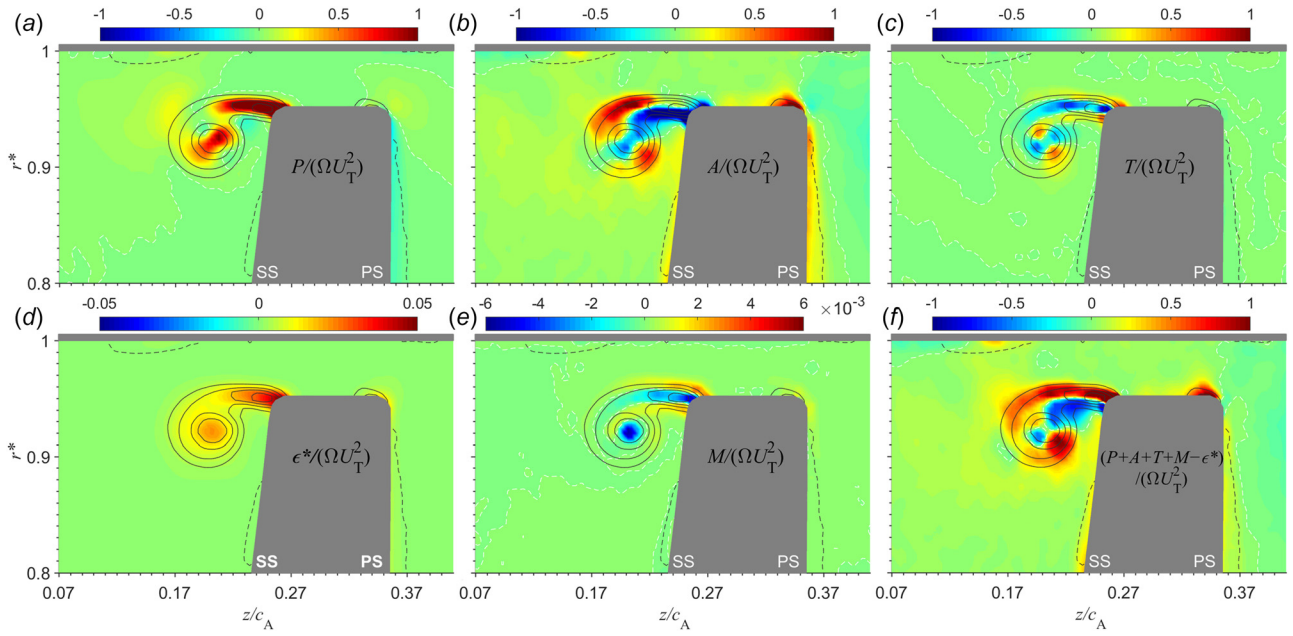

Fig. 7 Terms in the transport equation for TKE: (*a*) production rate, (*b*) advection by mean flow, (*c*) turbulent transport, (*d*) dissipation rate (underestimated), (*e*) viscous diffusion, and (*f*) $P + A + T + M - \varepsilon^*$

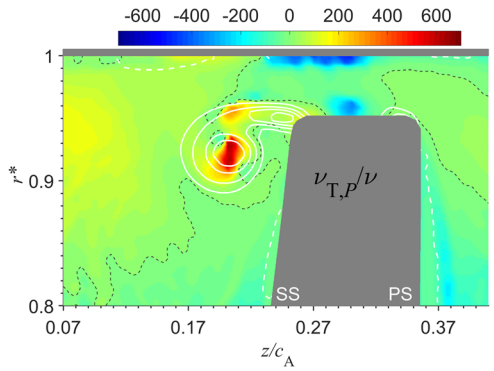

Fig. 8 Distribution of production-based eddy viscosity. Dashed contour lines follow the locations of zero values.

$$\rho_{RS} = \frac{|\boldsymbol{R}_{ij}^D \boldsymbol{S}_{ij}|}{|\boldsymbol{R}_{ij}^D \boldsymbol{R}_{ij}^D|^{\frac{1}{2}} |\boldsymbol{S}_{ij} \boldsymbol{S}_{ij}|^{\frac{1}{2}}} \tag{15}$$

to evaluate the correlation between $\boldsymbol{S}_{ij}$ and the deviatoric part of the Reynolds stresses $\boldsymbol{R}_{ij}^D$. The result is shown in Fig. 10. When there is a good correlation between the two tensors, the value of ρ_{RS} approaches 1, and when the correlation is poor, it approaches zero. As is evident, far from the tip region, in the area occupied by newly arriving main passage flow, $\boldsymbol{S}_{ij}$ and $\boldsymbol{R}_{ij}^D$ are indeed well correlated. Conversely, the correlation either fluctuates significantly or has near zero values in significant fractions of the tip region, strongly suggesting that the eddy viscosity concept, which assumes local equilibrium conditions, is inherently improper for modeling the Reynolds stresses in the rapidly strained tip region. Modeling of each of the Reynolds stresses individually using RSM might lead to more reasonable predictions, as confirmed by Uzol et al. [7] and Liu et al. [8] for turbomachinery flows.

One of the questions associated with the present analysis involves the impact of the Reynolds stresses (properly or improperly modeled) on the mean flow dynamics. One possible approach is to compare the divergence of the measured Reynolds stresses to the distributions of mean flow advection. As an example, Fig. 11 compares the distributions of $(U \cdot \nabla)U_z$ to that of $(\nabla \cdot \boldsymbol{R}^{\mathrm{D}})_z$. One should note the difference in scales. Evidently, for most of the tip flow, the mean flow advection is an order of magnitude larger than the corresponding Reynolds stress divergence, indicating the dominance of advection and pressure gradients. However, as the ratio between them (Fig. 11(*c*)) indicates, the Reynolds stress term is of comparable magnitude to the mean flow advection in the shear layer. Therefore, proper modeling of the Reynolds stresses would be critical for this region.

Conclusions

High-resolution measurements performed in a series of closely spaced planes in the tip region of an axial compressor provide a comprehensive database on the flow structure and turbulence characteristics there. The latter includes the distributions of all the components of Reynolds stress tensor, along with parameters affecting them, such as production, advection, and diffusion rates. For the current tip clearance and relatively high flow rate, the TLV and associated region of elevated turbulence remain located close to the blade SS tip corner, and the flow is not disrupted by large-scale instabilities. Significant high turbulence levels are measured in the vicinity of the TLV center and in the shear layer connecting it to the blade SS tip corner. Decomposition of TKE into three Reynolds normal stresses reveals high anisotropy, with $\langle u'^2_z \rangle$ peaking in the shear layer, $\langle u'^2_r \rangle$ dominating the vicinity of the TLV center, and $\langle u'^2_\theta \rangle$ being significantly smaller. Qualitatively, similar trends are also observed in other axial turbomachines, e.g., see Ref. [18], in spite of variations in the load distributions. The distributions of corresponding production rate terms can explain some of the trends. For example, the peak

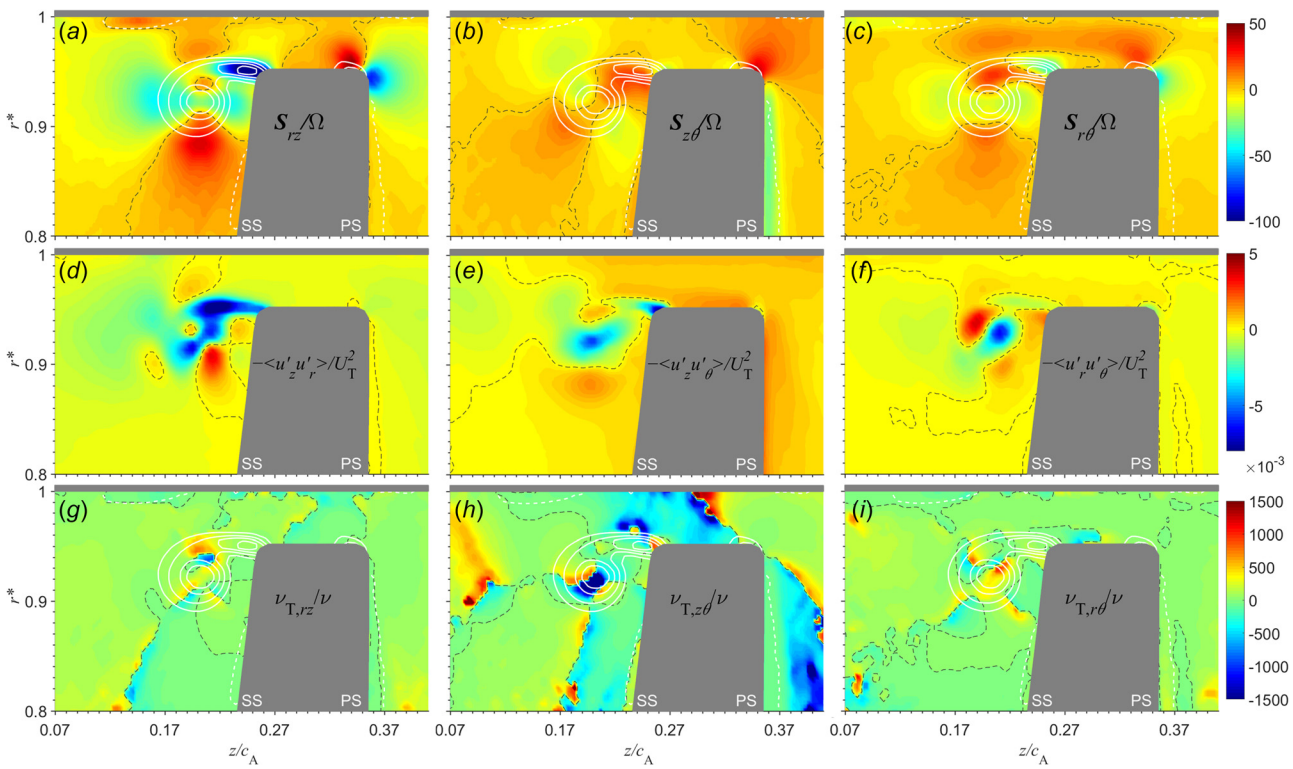

Fig. 9 Distributions of: (top row) mean shear strain rate components; (middle row) Reynolds shear stresses, and (bottom row) corresponding eddy viscosity: (*a*) S_{rz}, (*b*) $S_{z\theta}$, (*c*) $S_{r\theta}$, (*d*) $-\langle u'_r u'_z \rangle$, (*e*) $-\langle u'_z u'_\theta \rangle$, (*f*) $-\langle u'_r u'_\theta \rangle$, (*g*) $\nu_{T,rz}$, (*h*) $\nu_{T,z\theta}$, and (*i*) $\nu_{T,r\theta}$. Dashed lines follow the locations of zero values.

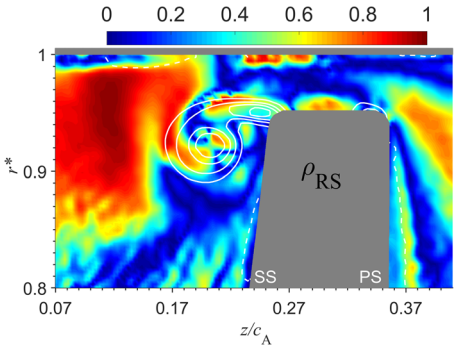

Fig. 10 Distribution of the ratio indicator ρ_{RS}

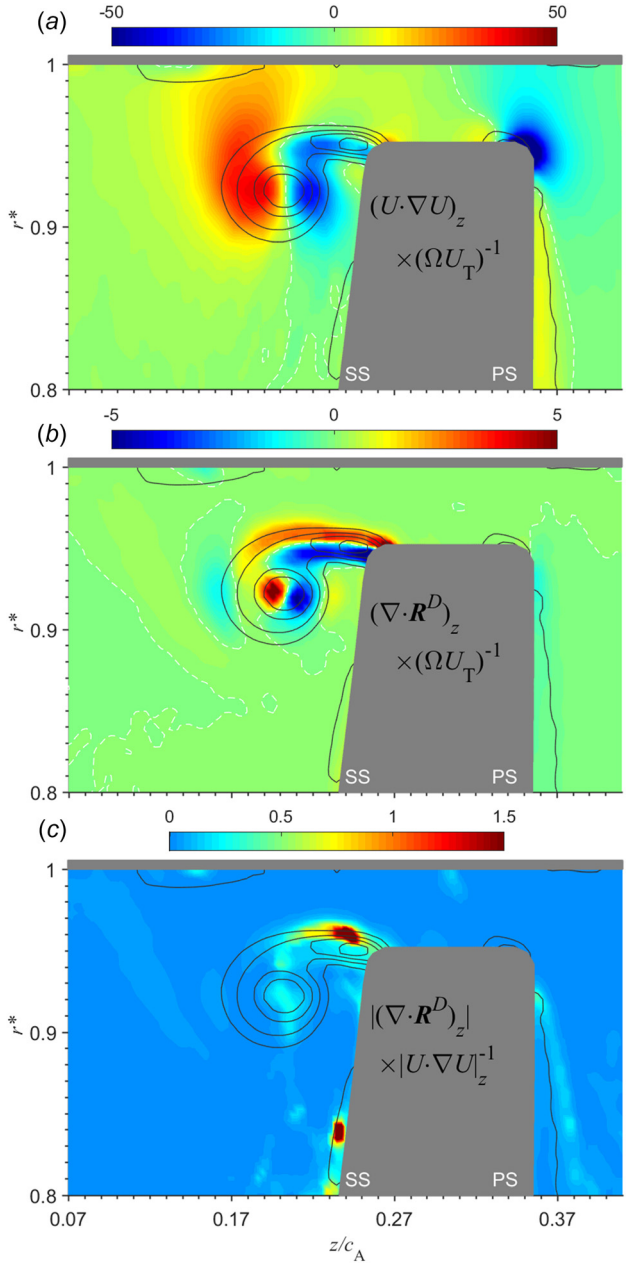

Fig. 11 Distributions of (*a*) mean advection term for axial velocity, (*b*) the corresponding divergence of measured deviatoric Reynolds stresses, and (*c*) the magnitude ratio between them

of $\langle u_z'^2 \rangle$ in the shear layer is associated with high shear production, and the elevated $\langle u_r'^2 \rangle$ in the TLV center corresponds to high radial contraction. The axial contraction near the SS tip corner as well as the radial and circumferential shear production in the vicinity of the TLV also contributes to the high turbulence level in these regions. However, some of the trends cannot be explained by the local production, requiring evaluations of other terms in the evolution equations of the corresponding stresses. Hence, other terms in the transport equation of TKE, such as mean-flow advection, turbulent transport and viscous diffusion, are also presented. The production rate, advection by mean flow, and turbulent transport appear to be significant contributors. Unfortunately, the present data do not have sufficient spatial resolution for calculating the dissipation rate, but it should also be a major component in the Reynolds stress dynamics. The discussion also leads to the conclusion that the pressure diffusion term, which is not calculated directly, should also play a significant role around the shear layer, especially in the region where the TLV-induced flow impinges on blade surfaces. Recently introduced techniques [41–45], using time-resolved 3D velocity to calculate the instantaneous pressure distribution, could be adopted for turbomachinery flows in future studies.

The applicability of popular turbulence models based on eddy viscosity is evaluated by several means. Both the production-based eddy viscosity and those directly estimated from the stress–strain rate relation reveal high spatial variation in sign and magnitude. These inconsistencies, along with the existence of several flow regions with negative stress production rates, indicate the prevalence of nonequilibrium conditions, where the Reynolds stresses and mean strain rates are poorly correlated. Although the Reynolds stress divergence terms are for the most part much smaller than the mean advection terms in the RANS equations, their magnitudes are comparable in high shear region, indicating the significance of proper Reynolds stress modeling. Such modeling is particularly challenging in the tip region. It should be noted that the present findings do not account for effects of compressibility. Hence, they are relevant to the rear stages of compressors.

Acknowledgment

The authors would like to thank Chunill Hah and Michael Hathaway from NASA Glenn for their guidance and for modifying the LSAC blade geometries to satisfy the constraints of the JHU refractive index-matched liquid facility. We would also like to express our gratitude to Yury Ronzhes for designing all the mechanical parts of this machine.

Funding Data

- Glenn Research Center (Grant No. NNX11AI21A).
- Office of Naval Research (Grant No. N00014-09-1-0353).

Nomenclature

A = advection rate
c = rotor blade tip chord
c_A = rotor blade tip axial chord
d = hub diameter
h = width of the rotor blade tip gap
i, j = indices for tensor notation (summation convention applied)
k = turbulent kinetic energy
L = distance from the hub surface to the inner casing endwall
M = viscous diffusion rate
p = static pressure
P = production rate
Q = volumetric flow rate
r^* = normalized radial coordinate

$\boldsymbol{R}^D$ = deviatoric part of Reynolds stress tensor
r, z, θ = radial, axial and circumferential coordinates
s = rotor blade chordwise coordinate
$\boldsymbol{S}$ = strain rate tensor
T = turbulent diffusion rate
U_T = rotor blade tip speed
u_r, u_z, u_θ = radial, axial and circumferential velocity
U_r, U_z, U_θ = ensemble-averaged radial, axial and circumferential velocity
u'_r, u'_z, u'_θ = fluctuating radial, axial and circumferential velocity components
V_z = volumetric flow rate divided by the annular through-flow area
α, β = indices for tensor notation (summation convention NOT applied)
ε = dissipation rate
ν = kinematic viscosity
ν_T = eddy viscosity
Π = pressure diffusion rate
ρ = density
φ = flow coefficient
ψ_{SS} = static-to-static pressure coefficient
Ω = rotor angular velocity
$\omega_r, \omega_z, \omega_\theta$ = radial, axial and circumferential vorticity
$\langle\ \rangle$ = ensemble average

References

[1] Lakshminarayana, B., 1986, "Turbulence Modeling for Complex Shear Flows," AIAA J., **24**(12), pp. 1900–1917.
[2] Lakshminarayana, B., 1991, "An Assessment of Computational Fluid Dynamic Techniques in the Analysis and Design of Turbomachinery—The 1990 Freeman Scholar Lecture," ASME J. Fluids Eng., **113**(3), pp. 315–352.
[3] Bradshaw, P., 1996, "Turbulence Modeling With Application to Turbomachinery," Prog. Aerosp. Sci., **32**(6), pp. 575–624.
[4] Tucker, P. G., 2013, "Trends in Turbomachinery Turbulence Treatments," Prog. Aerosp. Sci., **63**, pp. 1–32.
[5] Denton, J. D., 2010, "Some Limitations of Turbomachinery CFD," ASME Paper No. GT2010-22540.
[6] Denton, J. D., 1997, "Lessons From Rotor 37," J. Therm. Sci., **6**(1), pp. 1–13.
[7] Uzol, O., Brzozowski, D., Chow, Y.-C., Katz, J., and Meneveau, C., 2007, "A Database of PIV Measurements Within a Turbomachinery Stage and Sample Comparisons With Unsteady RANS," J. Turbul., **8**, p. N10.
[8] Liu, Y., Yu, X., and Liu, B., 2008, "Turbulence Models Assessment for Large-Scale Tip Vortices in an Axial Compressor Rotor," J. Propul. Power, **24**(1), pp. 15–25.
[9] Moore, J. G., and Moore, J., 1999, "Realizability in Turbulence Modelling for Turbomachinery CFD," ASME Paper No. 99-GT-024.
[10] Durbin, P. A., 1996, "On the k-3 Stagnation Point Anomaly," Int. J. Heat Fluid Flow, **17**(1), pp. 89–90.
[11] Shabbir, A., Zhu, J., and Celestina, M., 1996, "Assessment of Three Turbulence Models in a Compressor Rotor," ASME Paper No. 96-GT-198.
[12] Horlock, J. H., and Denton, J. D., 2005, "A Review of Some Early Design Practice Using Computational Fluid Dynamics and a Current Perspective," ASME J. Turbomach., **127**(1), pp. 5–13.
[13] Lakshminarayana, B., Davino, R., and Pouagare, M., 1982, "Three-Dimensional Flow Field in the Tip Region of a Compressor Rotor Passage—Part II: Turbulence Properties," ASME J. Eng. Power, **104**(4), pp. 772–781.
[14] Muthanna, C., and Devenport, W. J., 2004, "Wake of a Compressor Cascade With Tip Gap—Part 1: Mean Flow and Turbulence Structure," AIAA J., **42**(11), pp. 2320–2331.
[15] Wang, Y., and Devenport, W. J., 2004, "Wake of a Compressor Cascade With Tip Gap—Part 2: Effects of Endwall Motion," AIAA J., **42**(11), pp. 2332–2340.
[16] You, D., Wang, M., Moin, P., and Mittal, R., 2007, "Large-Eddy Simulation Analysis of Mechanisms for Viscous Losses in a Turbomachinery Tip-Clearance Flow," J. Fluid Mech., **586**, pp. 177–204.
[17] You, D., Wang, M., Moin, P., and Mittal, R., 2006, "Effects of Tip-Gap Size on the Tip-Leakage Flow in a Turbomachinery Cascade," Phys. Fluids, **18**(10), p. 105120.
[18] Wu, H., Miorini, R. L., Tan, D., and Katz, J., 2012, "Turbulence Within the Tip-Leakage Vortex of an Axial Waterjet Pump," AIAA J., **50**(11), pp. 2574–2587.
[19] Wu, H., Tan, D., Miorini, R. L., and Katz, J., 2011, "Three-Dimensional Flow Structures and Associated Turbulence in the Tip Region of a Waterjet Pump Rotor Blade," Exp. Fluids, **51**(6), pp. 1721–1737.
[20] Wu, H., Miorini, R. L., and Katz, J., 2011, "Measurements of the Tip Leakage Vortex Structures and Turbulence in the Meridional Plane of an Axial Water-Jet Pump," Exp. Fluids, **50**(4), pp. 989–1003.
[21] Borello, D., Delibra, G., Hanjalić, K., and Rispoli, F., 2009, "Large-Eddy Simulations of Tip Leakage and Secondary Flows in an Axial Compressor Cascade Using a Near-Wall Turbulence Model," Proc. Inst. Mech. Eng., Part A, **223**(6), pp. 645–655.
[22] Hah, C., Hathaway, M., and Katz, J., 2014, "Investigation of Unsteady Flow Field in a Low-Speed One and a Half Stage Axial Compressor—Part 2: Effects of Tip Gap Size on the Tip Clearance Flow Structure at Near Stall Operation," ASME Paper No. GT2014-27094.
[23] Hah, C., Hathaway, M., Katz, J., and Tan, D., 2015, "Investigation of Unsteady Tip Clearance Flow in a Low-Speed One and Half Stage Axial Compressor With LES and PIV," ASME Paper No. AJKFluids2015-2061.
[24] Tan, D., Li, Y., Wilkes, I., Miorini, R. L., and Katz, J., 2014, "Visualization and Time Resolved PIV Measurements of the Flow in the Tip Region of a Subsonic Compressor Rotor," ASME Paper No. GT2014-27195.
[25] Tan, D., Li, Y., Wilkes, I., Miorini, R. L., and Katz, J., 2014, "PIV Measurements of the Flow in the Tip Region of a Compressor Rotor," ASME Paper No. FEDSM2014-21593.
[26] Tan, D., Li, Y., Chen, H., Wilkes, I., and Katz, J., 2015, "The Three Dimensional Flow Structure and Turbulence in the Tip Region of an Axial Flow Compressor," ASME Paper No. GT2015-43385.
[27] Li, Y., Tan, D., Chen, H., and Katz, J., 2015, "Effects of Tip Gap Size on the Flow Structure in the Tip Region of an Axial Turbomachine," ASME Paper No. AJKFluids2015-33787.
[28] Li, Y., Chen, H., Tan, D., and Katz, J., 2016, "Effects of Tip Clearance and Operating Conditions on the Flow Structure and Turbulence Within an Axial Compressor Rotor Passage," ASME Paper No. GT2016-57050.
[29] Chen, H., Li, Y., Tan, D., and Katz, J., 2017, "Visualizations of Flow Structures in the Rotor Passage of an Axial Compressor at the Onset of Stall," ASME J. Turbomach., **139**(4), p. 041008.
[30] Wisler, D. C., 1977, "Core Compressor Exit Stage Study—Volume I: Blade Design," NASA Lewis Research Center, Cleveland, OH, NASA Technical Report No. NASA CR135391.
[31] Wasserbauer, C. A., Weaver, H. F., and Senyitko, R. G., 1995, "NASA Low-Speed Axial Compressor for Fundamental Research," NASA Lewis Research Center, Cleveland, OH, NASA Technical Report No. NASA-TM-4635.
[32] Wieneke, B., 2005, "Stereo-PIV Using Self-Calibration on Particle Images," Exp. Fluids, **39**(2), pp. 267–280.
[33] Roth, G. I., and Katz, J., 2001, "Five Techniques for Increasing the Speed and Accuracy of PIV Interrogation," Meas. Sci. Technol., **12**(3), pp. 238–245.
[34] Özcan, O., Meyer, K. E., and Larsen, P. S., 2005, "Measurement of Mean Rotation and Strain-Rate Tensors by Using Stereoscopic PIV," Exp. Fluids, **39**(4), pp. 771–783.
[35] Uzol, O., Chow, Y. C., Katz, J., and Meneveau, C., 2002, "Unobstructed PIV Measurements Within an Axial Turbo-Pump Using Liquid and Blades With Matched Refractive Indices," Exp. Fluids, **33**(6), pp. 909–919.
[36] Miorini, R. L., Wu, H., and Katz, J., 2012, "The Internal Structure of the Tip Leakage Vortex Within the Rotor of an Axial Waterjet Pump," ASME J. Turbomach., **134**(3), p. 031018.
[37] Lumley, J. L., 1979, "Computational Modeling of Turbulent Flows," Adv. Appl. Mech., **18**, pp. 123–176.
[38] Simonsen, A. J., and Krogstad, P. Å., 2005, "Turbulent Stress Invariant Analysis: Clarification of Existing Terminology," Phys. Fluids, **17**(8), p. 088103.
[39] Banerjee, S., Krahl, R., Durst, F., and Zenger, C., 2007, "Presentation of Anisotropy Properties of Turbulence, Invariants Versus Eigenvalue Approaches," J. Turbul., **8**, p. N32.
[40] Lakshminarayana, B., 1996, *Fluid Dynamics and Heat Transfer of Turbomachinery*, Wiley, New York.
[41] Liu, X., and Katz, J., 2006, "Instantaneous Pressure and Material Acceleration Measurements Using a Four-Exposure PIV System," Exp. Fluids, **41**(2), pp. 227–240.
[42] Liu, X., and Katz, J., 2013, "Vortex-Corner Interactions in a Cavity Shear Layer Elucidated by Time-Resolved Measurements of the Pressure Field," J. Fluid Mech., **728**, pp. 417–457.
[43] Charonko, J. J., King, C. V., Smith, B. L., and Vlachos, P. P., 2010, "Assessment of Pressure Field Calculations From Particle Image Velocimetry Measurements," Meas. Sci. Technol., **21**(10), p. 105401.
[44] de Kat, R., and van Oudheusden, B. W., 2012, "Instantaneous Planar Pressure Determination From PIV in Turbulent Flow," Exp. Fluids, **52**(5), pp. 1089–1106.
[45] Zhang, C., Wang, J., Blake, W., and Katz, J., 2017, "Deformation of a Compliant Wall in a Turbulent Channel Flow," J. Fluid Mech., **823**, pp. 345–390.
[46] Soranna, F., Chow, Y.-C., Uzol, O., and Katz, J., 2006, "The Effect of Inlet Guide Vanes Wake Impingement on the Flow Structure and Turbulence Around a Rotor Blade," ASME J. Turbomach., **128**(1), pp. 82–95.
[47] Xu, D., and Chen, J., 2013, "Accurate Estimate of Turbulent Dissipation Rate Using PIV Data," Exp. Therm. Fluid Sci., **44**, pp. 662–672.
[48] Delafosse, A., Collignon, M. L., Crine, M., and Toye, D., 2011, "Estimation of the Turbulent Kinetic Energy Dissipation Rate From 2D-PIV Measurements in a Vessel Stirred by an Axial Mixel TTP Impeller," Chem. Eng. Sci., **66**(8), pp. 1728–1737.
[49] Luznik, L., Gurka, R., Nimmo-Smith, W. A. M., Zhu, W., Katz, J., and Osborn, T. R., 2007, "Distribution of Energy Spectra, Reynolds Stresses, Turbulence Production, and Dissipation in a Tidally Driven Bottom Boundary Layer," J. Phys. Oceanogr., **37**(6), pp. 1527–1550.
[50] Soranna, F., Chow, Y.-C., Uzol, O., and Katz, J., 2008, "Turbulence Within a Turbomachine Rotor Wake Subject to Nonuniform Contraction," AIAA J., **46**(11), pp. 2687–2702.
[51] Schmitt, F. G., 2007, "About Boussinesq's Turbulent Viscosity Hypothesis: Historical Remarks and a Direct Evaluation of Its Validity," C. R. Mec., **335**(9–10), pp. 617–627.